ChemPubSoc Europe

DOI: 10.1002/cphc.201800473

CHEMPHYSCHEM Articles

# Monolayer $AsTe_2$: Stable Robust Metal in 2D, 1D and 0D

S. V. Badalov,*[a] A. Kandemir,[b] and H. Sahin[a, c]

The structural, phononic, and electronic properties of the monolayer structures of $AsTe_2$ are characterized by performing density functional theory (DFT) calculations. Total energy optimization and phonon calculations reveal that single layers of the 2H-$AsTe_2$ and 1T-$AsTe_2$ phases form dynamically stable crystal structures. Electronic structure analysis also shows that both 2H and 1T phases have nonmagnetic metallic character. It is also predicted that the metallic nature of the ultra-thin both 2H-$AsTe_2$ and 1T-$AsTe_2$ structures remain unchanged even under high biaxial strain values. For further examination of the dimensionality effect in the robust metallicity in 2D $AsTe_2$ phases, electronic characteristics of 1D nanoribbons and 0D quantum dots are also investigated. It is found that independent from the dimension and crystallographic orientations 0D and 1D structures of 2H- and 1T-$AsTe_2$ structures have metallic behavior. It is found that single layers of $AsTe_2$ are quite promising materials for nanodevice applications owing to the robust metallic character.

## 1. Introduction

After the synthesis of graphene,[1,2] two-dimensional (2D) materials have induced the world-wide scientific and technological interest with their unconventional properties for the development of modern electronics. These novel materials such as hexagonal boron nitride (h-BN),[3–5] silicene,[6,7] transition metal dichalcogenides (TMDs),[8–11] metallic surfactant-capped Pd,[12] Rh nanosheets,[13] and group-15 materials such as phosphorene, arsenene, antimonene and bismuthene[14–19] were successfully synthesized over past decade.

Depending on the number of *d*-electrons on metal atoms, TMDs may display various electronic characteristics from semiconducting to metallic or superconducting states.[10] 1T phase TMDs have received much attention owing to their large surface area, good electrical conductivity, excellent catalytic activity and low cost compared to noble metals.[20] Hence, the development of 2D metals with desirable physical intriguing properties is of so significance, particularly for the biosensing and imaging,[12,21] band pass and band stop filters in photonic crystals,[22,23] high efficiency field-effect transistors,[24] catalysis,[13] magnetic recording,[25] metal-semiconductor junction,[26] thermoelectric,[27,28] and superconducting applications.[29]

In addition, bulk forms of group-15 sesquichalcogenides with generic formula $A_2X_3$ (A=As, Sb, Bi; X=S, Se, Te) have been widely investigated owing to their distinguishable thermoelectric properties[30,31] and 3D topological insulator character.[32,33] Among these, several types of phases of bulk Arsenic Telluride ($As_2Te_3$) have been widely studied.[34–36] Its unique physical characteristics such as structural transformation by heat and pressure,[36,37] high power factors and low thermal conductivity,[38] and variety multicomponent amorphous/glass-ceramics system[38] allowed to be used in the application of thermoelectric,[34,35,38,39] threshold and memory switching,[35,40] and pressure-induced metalization.[36] Platakis *et al.* reported that the $As_2Te_3$ crystalline form is far better suited for memory switching device applications than the amorphous $As_2Te_3$.[35] Vaney *et al.* reported the thermoelectric characterization of the compound $\alpha$-$As_2Te_3$ between 5 K and 523 K.[38] It was shown that $\alpha$-$As_2Te_3$ has $\sim$1 W m$^{-1}$ K$^{-1}$ thermal conductivity around room temperature which is lower than $SiO_2$ thin layer.[41,42] Very recently, the PECVD synthesis and optical characterization of As–Te chalcogenide films were successfully done by Mochalov *et al.*[43–46] It was found that the degree of transparency and the surface roughness of the deposited films increase with increasing of the Te content. Furthermore, the electronic structures and vibrational properties of the layered $\alpha$phase $As_2Te_3$ was studied under compression.[47] However, compared to widely studies in 3D form $As_2Te_3$, monolayer forms had not been investigated so far.

In this study, we report two unexplored stable metal monolayer Arsenic Telluride phases: 2H-$AsTe_2$ and 1T-$AsTe_2$, and carry out the comprehensive analysis of their structural, phononic, and electronic properties. It is well-known that the synthesis of free-standing 2D materials with metallic bonding has remained elusive because of their close-packed structures, whereas the 2H and 1T polytypes of TMDs have covalent type bond.[20,48] In order to understand the electronic susceptibility of monolayers, electronic characteristics of 1D nanoribbons and 0D quantum dot flakes are also comprehensively studied with regards to size and crystallographic orientations. These two different ultra-thin robust metal materials can be exceedingly promising candidates for different electronic device application such as efficient thermoelectric devices, field-effect transistors, phase-change electronic devices.

The remainder of the paper is organized as follows: computational details are given in Sec. 2. Next, the structural,

[a] S. V. Badalov, H. Sahin
Department of Photonics, Izmir Institute of Technology, 35430 Izmir, Turkey
E-mail: sabuhibadalov@iyte.edu.tr
[b] A. Kandemir
Department of Materials Science and Engineering, Izmir Institute of Technology, 35430 Izmir, Turkey
[c] H. Sahin
ICTP-ECAR Eurasian Center for Advanced Research, Izmir Institute of Technology, 35430 Izmir, Turkey

vibrational, and electronic properties of the ultra-thin structures of $AsTe_2$ monolayers are presented in Sec. 3. In Sec. 4 and 5, 1D nanoribbons and 0D quantum dots of the 2H-$AsTe_2$ and 1T-$AsTe_2$ structures are studied in detail, respectively. Finally, the results are concluded in Sec. 6.

## 2. Computational Details

All the calculations were performed using the projector augmented wave (PAW) potentials as implemented in the Vienna *ab initio* Simulation Package (VASP).[49,50] The local density approximation (LDA)[51] was used to describe the exchange and correlation potential as parametrized by the Ceperley-Alder functional.[52] Analyzes of the charge transfers between bonding atoms were determined by the Bader technique.[53]

The size of the plane-wave basis set was limited with kinetic energy cutoff of 500 eV. The convergence criterion for total energy was taken to be $10^{-5}$ eV between the sequential steps and Hellmann-Feynman forces on each unit cell was less than $10^{-4}$ eV/Å. $18\times18\times1$ $\Gamma$-centered k-point sampling was used for the primitive unit cell for band structure calculation with the spin-polarized case in terms of spin-orbit coupling (SOC). The Methfessel-Paxton scheme broadening for the density of states calculation was taken to be 0.2. To avoid interactions between adjacent $AsTe_2$ monolayers, our calculations were performed with a large unit cell which were limited with ~16 Å vacuum region along the out-of-plane direction. Phonon dispersions and eigenvectors were calculated by making use of small displacement method (SDM) in the PHON code.[54] The cohesive energy per atom $E_{Coh}/n_{tot}$was calculated by using the formula as $E_{Coh}/n_{tot} = [n_{As}E_{As} + n_{Te}E_{Te} - E_{ML}]/n_{tot}$, where $E_{As}$ and $E_{Te}$ represent, respectively, the energies of single isolated As and Te atoms. $E_{ML}$ stands for the total energy of the 2H- and 1T-$AsTe_2$ structures, $n_{tot}$, $n_{As}$and $n_{Te}$denote the total number of atoms, number of As and Te atoms within in the unit cell, respectively.

## 3. 2D $AsTe_2$ Monolayer Structures

### 3.1. Structural Phases of $AsTe_2$ Monolayers

The optimized atomic structures of the trigonal prismatic and octahedral coordination forming 2H and 1T polytypes of $AsTe_2$, respectively, are shown in Figure 1(a) and (b). As given in Table 1, the lattice parameters of the optimized crystal structures of primitive unit cell of 2H and 1T phases are 3.60 and 3.74 Å, respectively. 2H and 1T phases, respectively, belong to P6*m*2and P$\bar{3}$*m*1space groups, with the hexagonal Bravais lattice. The bond distances between As and Te atoms for 2H and 1T phases are 2.84 and 2.80 Å, respectively. The thicknesses of monolayer 2H and 1T phases of $AsTe_2$ structure, which is defined to be the vertical distance between uppermost and lowermost Te atom, are 3.87 and 3.58 Å, respectively.

It is found that the 1T-$AsTe_2$ structure has a relatively lower ground state energy (~0.3 eV) with respect to the 2H, and this small ground state energy difference allows one to synthesize both of phase as a coplanar. Bader charge analysis reveals that As atom donates $0.1e^-$ to each Te atom in 2H-$AsTe_2$ and 1T-$AsTe_2$ monolayers, i.e., the polar character is observed in both phases of $AsTe_2$ in addition to the covalent type bonds. Regarding the cohesive energies of 2H and 1T phases, the 1T-$AsTe_2$ structure is the most favorable structure, with a higher cohesive energy of 0.09 eV/atom with respect to the 2H. As a given in Table 1, the 2H-$AsTe_2$ and 1T-$AsTe_2$ structures' work functions are, respectively, 4.78 and 4.94 eV which are very close to work function (WF) of graphene (~4.6 eV).[55] Both ground state structures of the $AsTe_2$ phases are found to be nonmagnetic.

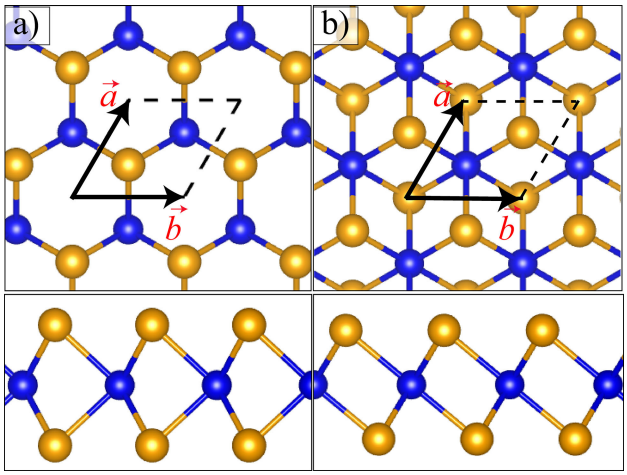


**Figure 1.** (Color online) Top and side views of geometric structure of (a) 2H-$AsTe_2$ and (b) 1T-$AsTe_2$ monolayers. The black vectors stand for unit cell vectors. Dark blue and orange spheres represent As and Te atoms, respectively.

**Table 1.** The calculated parameters for monolayers of 2H-$AsTe_2$ and 1T-$AsTe_2$ are; the lattice constants, $a = b$; the atomic distance between As and Te atoms, $d_{As\text{-}Te}$; the thickness of monolayer, t; the charge donation of As, $\Delta\rho$; the cohesive energy per atom, $E_{Coh}$; $\Phi$ and $\mu$ are the values of work function and magnetization, respectively.

| | $a$ (Å) | $d_{As\text{-}Te}$ (Å) | t (Å) | $\Delta\rho$ ($e^-$) | $E_{Coh}$ (eV) | $\Phi$ (eV) | $\mu$ ($\mu_B$) |
|---|---|---|---|---|---|---|---|
| 2H-$AsTe_2$ | 3.60 | 2.84 | 3.87 | 0.1 | 3.30 | 4.78 | 0 |
| 1T-$AsTe_2$ | 3.74 | 2.80 | 3.58 | 0.1 | 3.39 | 4.94 | 0 |

### 3.2. Phonons: Dynamical Stability

The dynamical stability of the monolayers of 2H-$AsTe_2$ and 1T-$AsTe_2$ is studied by examining the phonon spectra of the crystals. In 2H-$AsTe_2$ and 1T-$AsTe_2$ monolayers, the unit cells are composed of three atoms (two tellurium and one arsenic atoms) with three acoustic and six optical vibrational modes at the $\Gamma$point based on $D_{3h}$ and $D_{3d}$ symmetries, respectively. Hence, the decomposition of the vibration representation is calculated to be $\Gamma = 2E'' + 2E' + A'_1 + A''_2$ and $\Gamma = 2E_g + 2E_u + A_{1g} + A_{2u}$ for monolayers of 2H-$AsTe_2$ and 1T-$AsTe_2$, respectively.

2H-$AsTe_2$ monolayer has $A''_2$ (146 $cm^{-1}$) and $A'_1$ (140 $cm^{-1}$) out-of-plane phonon modes, and two doubly degenerate $E'$ (118 $cm^{-1}$) and $E''$ (66 $cm^{-1}$) in-plane modes. The optical vibrational modes of 1T-$AsTe_2$ monolayer at the $\Gamma$consist two non-degenerate out-of-plane modes: $A_{2u}$ (192 $cm^{-1}$) and $A_{1g}$ (131 $cm^{-1}$), and two doubly degenerate in-plane modes: $E_u$ (110 $cm^{-1}$) and $E_g$ (92 $cm^{-1}$). The corresponding eigenvectors of optical modes of 2H-$AsTe_2$ and 1T-$AsTe_2$ are illustrated in Figure 2. Among the modes, the $E''$, $A'_1$, $E_g$ and $A_{1g}$ modes are

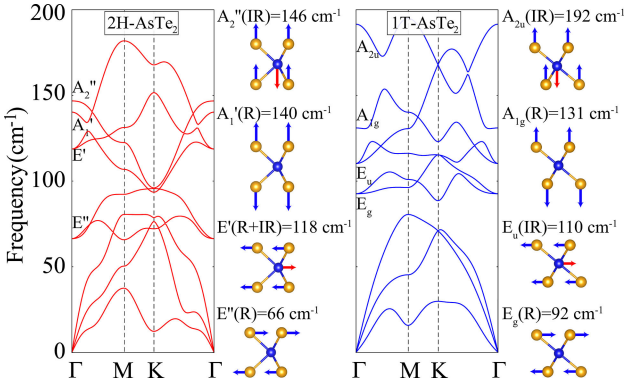


**Figure 2.** (Color online) The phonon dispersions of 2H-$AsTe_2$ and 1T-$AsTe_2$ monolayers. The red line and blue line represent, respectively, the phononic band diagrams of 2H-$AsTe_2$ and 1T-$AsTe_2$ monolayers. Side views of eigenvectors correspond to related with optical phonon modes are shown as well.

Raman active, $A''_2$, $E_u$ and $A_{2u}$ modes are Infrared active, and $E'$ mode is both Raman and Infrared active.

As it is clearly seen from Figure 2, 2H- and 1T-$AsTe_2$ monolayers are dynamically stable because all phonon modes have real eigenfrequencies; thus, it is shown that synthesis of both phases is possible as a free-standing monolayer via bottom-up approaches: chemical vapor deposition and atomic or molecular condensation methods, allowing the As and Te as precursors to grow in size.[43–46] Furthermore, due to atomic masses, the phonon modes of 2H-$AsTe_2$ and 1T-$AsTe_2$ monolayers lie at low frequencies smaller than 200 $cm^{-1}$, which indicate that both of them are softer materials than other 2D materials such as $MoS_2$, graphene, h-BN.[56–58] It is well-known that the soft materials have the low thermal conductivity, namely, the predicted ultra-thin $AsTe_2$ structures can be utilized as the thermoelectric materials.[59]

### 3.3. Electronic Properties of $AsTe_2$ Monolayers

The electronic properties of the monolayers of 2H-$AsTe_2$ and 1T-$AsTe_2$ structures are investigated by analyzing the band structure and corresponding partial density of states (PDOS) as shown in Figure 3. It is found that both $AsTe_2$ phases possess electronically metallic character with the nonzero density of states at the Fermi level. By comparing electronic band diagrams of two phases, 2H-$AsTe_2$ monolayer has more metallic character than 1T-$AsTe_2$ monolayer structure, since six bands in

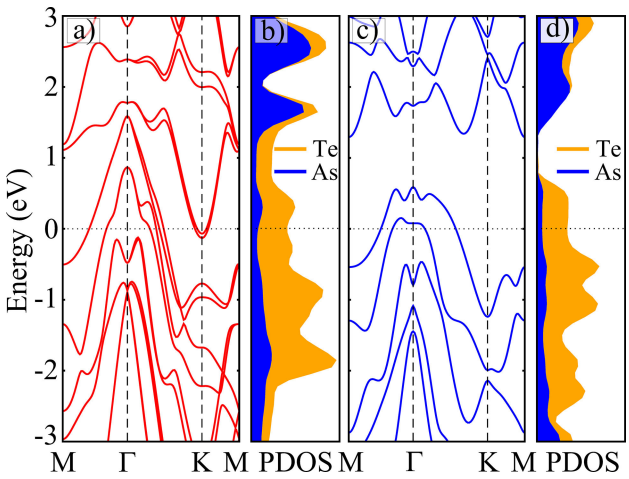


**Figure 3.** (Color online) (a) The electronic band diagram and (b) atom-decomposed electronic density of states of 2H-$AsTe_2$ monolayer. (c) The electronic band diagram and (d) atom-decomposed electronic density of states of 1T-$AsTe_2$ monolayer. The Fermi level is set to zero. The red line and blue line represent, respectively, the band diagram of 2H-$AsTe_2$ and 1T-$AsTe_2$.

2H-$AsTe_2$ and two bands in 1T-$AsTe_2$ cross the Fermi level. Furthermore, the PDOSs showed that Te atoms provide more contribution to both of $AsTe_2$ monolayers than As atoms around Fermi level [see Figure 3(b),(d)]. Although the negligible effect that spin-orbit coupling (SOC) has on the electronic structure in 2H-$AsTe_2$ monolayer, it is found that the spin-orbit splitting is ~190 *meV* in the highest valence band (VB) states at the K high symmetry point and ~60 *meV* in the lowest conduction band (CB) states at the K point in 2H-$AsTe_2$ monolayer. However, there is no spin-orbit splitting in 1T-$AsTe_2$ monolayer due to the inversion symmetry.

### 3.4. Strain Tolerance

The electronic properties and other associated features of 2D materials appear to be highly sensitive to the strain and environment because of the extreme thinness. For this reason, strain tolerance of the metallic character of the $AsTe_2$ phases is required to be investigated for determining its strain limits on possible device applications.

Therefore, 2H-$AsTe_2$ and 1T-$AsTe_2$ monolayers' electronic structures are studied by applying strain along biaxial, armchair, and zigzag directions. There is the much less significant effect of strain along armchair and zigzag direction in 2H- and 1T-$AsTe_2$. Thus, the electronic band diagrams of the biaxially strained $AsTe_2$ phases are illustrated in Figure 4. Compressive and tensile strain are applied up to 5%. There are six valence bands and two conduction bands crossing the Fermi level under compressive strain at the $\Gamma$ and the K high symmetry points in 2H-$AsTe_2$ monolayer. During the tension strain, the 2H-$AsTe_2$ structure remains almost same and the constituent orbitals of the highest VB and the lowest CB states are getting away a little bit from each other. Although 5% tension and compression strain is quite higher, the structures preserve their electronically metallic character, and slight small changes are

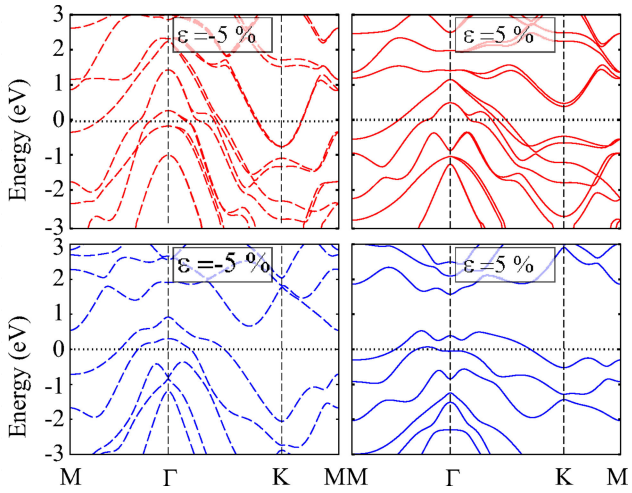


**Figure 4.** (Color online) The electronic band diagrams of 2H-$AsTe_2$ and 1T-$AsTe_2$ monolayers under compressive and tensile biaxial strain. The Fermi level is set to zero. The red and blue lines represent, respectively, the electronic band diagram of 2H-$AsTe_2$ and 1T-$AsTe_2$.

observed in 1T-$AsTe_2$ monolayer. Thereby, the influence of compressive and tensile strain to the electronic structure of 1T phase is the most visible from the $\Gamma$ to the K point, where both the bottom of conduction and the top of valence bands are slightly lowered and increased, respectively, compared with the equilibrium structure. Hereby, the electronic properties of 2H-$AsTe_2$ and 1T-$AsTe_2$ monolayers are generally an independent under mechanical deformation, namely, both of structures are the quite robust metallic materials, which keep the promise for different 2D electronic device applications such as the thermoelectric devices, field-effect transistors, and thin-film transistors.

## 4. 1D Nanoribbons of Ultra-thin $AsTe_2$

For nanoelectronic applications, it is important to investigate the electronic band structure of nanoribbons (NRs) which are dominated by the edge structure and ribbon width. While 2H-$AsTe_2$ and 1T-$AsTe_2$ monolayers are robust metallic materials, any application involving these materials may use only a small piece of them or a flake, not an infinite size. As well-known, the electronic character of graphene is changed from semimetal to semiconductor depending on the ribbon width,[60] and the electronic character of $MoS_2$ can be semiconductor or metal by adjusting the crystallographic orientation of nanoribbon edges.[61,62] For deeper understanding the robust metallic character of ultra-thin structures of the $AsTe_2$ phases, 1D types of the ultra-thin $AsTe_2$ structures are investigated in detail. Generally, nanoribbons (NRs) show band gap opening by decreasing the width size of the ribbons or edge construction as zigzag or armchair form; therefore, the narrowest scheme of the two crystallographic orientations of the 2H- and 1T-$AsTe_2$ NRs axis: armchair (ARM NR) and zigzag (ZZ NR) are studied.

All ground state structures of the narrowest $AsTe_2$ ARM and ZZ NRs are calculated to be nonmagnetic, and it is seen that the edge states have no effect on the magnetization of the structures. Our narrowest NR structures are formed without dangling bonds that provide to understand electronic characteristics intrinsically because it influences the electronic band dispersion and magnetism of structures as seen in well-known 2D materials such as graphene, silicene, and germanene.[6,63,64] In addition, the widths of the optimized structures of the narrowest $AsTe_2$ ARM and ZZ NRs are calculated to be in the range between ~5 and 7 Å. The electronic band diagrams of the narrowest NRs of the 2H- and 1T-$AsTe_2$ are depicted in Figure 5 with the top view of the NRs' structures. In the $AsTe_2$

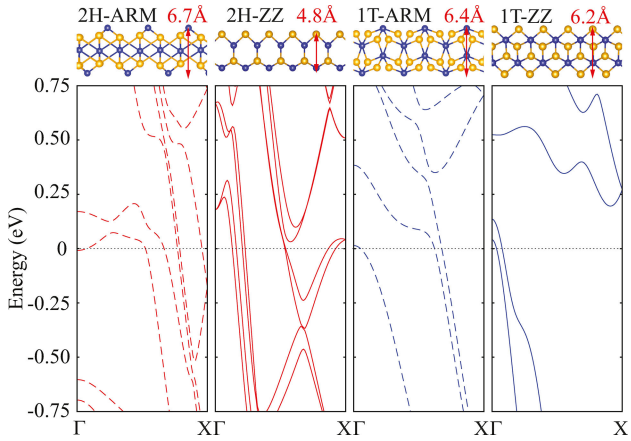


**Figure 5.** (Color online) The electronic band diagrams of 1D NRs of ultra-thin 2H and 1T-$AsTe_2$ structures in the armchair and zig-zag direction. The upper panel shows the top view representations of the armchair and zigzag NRs of the $AsTe_2$ phases. The Fermi level is set to zero. The red and blue lines represent, respectively, the electronic band diagrams of 1D NRs of 2H-$AsTe_2$ and 1T-$AsTe_2$.

ZZ NRs, no remarkable structural reconstruction is seen and the overall geometry of both monolayer phases is maintained. On the other hand, slightly disturbed hexagons in the structures are seen in the ARM NRs of $AsTe_2$. However, the electronic properties of the $AsTe_2$ ARM and ZZ NRs show no alteration and sustain the metallic character of the 2D $AsTe_2$ structures. Hence, the narrowest $AsTe_2$ ARM and ZZ NRs have disparate characteristics from the nanoribbons of other widely studied 2D materials such as graphene or $MoS_2$. Since the nanoribbons cut from 2D structures, it is shown that the strong metallic character of the $AsTe_2$ structures provides important contact features for various nanotechnology applications, even though the narrowest ones show no significant change in electronic character.

## 5. 0D Quantum Dots of Ultra-thin $AsTe_2$

To further understand the robust metallic character of 2H-$AsTe_2$ and 1T-$AsTe_2$ structures, the investigation of the electronic properties of quantum dot (QD) flakes is considered for both phases. Therefore, how the forbidden gaps between the highest energy occupied molecular orbital (HOMO) and the lowest energy unoccupied molecular orbital (LUMO) vary

depending on the size of the triangular QD flakes of 2H-$AsTe_2$ and 1T-$AsTe_2$ structures are investigated in detail.

As a result of the crystal symmetry of 2H and 1T phases formation of triangle shape is preferred in two-dimensional nanoflakes.[65–67] Therefore, the HOMO-LUMO energy states of the triangular QDs of the 2H- and 1T-$AsTe_2$ structures as a function of both size and phase are presented in Figure 6.

Firstly, we construct the 2H-$AsTe_2$ triangular QD flakes with consisting of three, six, ten and fifteen hexagons. Apart from minor bond contractions of the edge atoms, 2H-$AsTe_2$ triangular QD flakes preserve their hexagonal structures. As seen in Figure 6, there are different kinds of corner edge reconstructions, depending on whether As or Te atoms are located on the edge of triangular QD flakes. It is found that these structures are formed without dangling bonds. The HOMO-LUMO energy states vary distinctly with depending on corner edge reconstruction in 2H-$AsTe_2$ triangular QD flakes: thus, while As atoms situate in corner of QD flakes (see $2^{nd}$, $4^{th}$, and $6^{th}$ 2H-$AsTe_2$ QD flakes in Figure 6), their HOMO-LUMO energy gaps are found. However, while Te atoms in corner of QD flakes (see $1^{st}$, $3^{rd}$, $5^{th}$ and $7^{th}$ 2H-$AsTe_2$ QD flakes in Figure 6), QD flakes possess electronically metallic character. While the size of triangle 2H-$AsTe_2$ QD flakes with As terminated edge increases, the HOMO-LUMO energy gap starts getting a little bit larger with comparing previous one. However, the HOMO-LUMO energy gap goes on getting smaller and being completely metallic in next step. Furthermore, according to the cohesive energies of 2H-$AsTe_2$ triangular QD flakes, the formation of QDs with Te terminated edge requires higher cohesive energy (~0.14 eV/atom) than As terminated ones, i.e., the metal QDs are more favorable.

Owing to the structure of 1T-$AsTe_2$, there is the possibility to form many kinds of triangular QD flakes with comparing 2H phases. Unlike 2H structures, hexagons of some 1T-$AsTe_2$ QD flakes are not well-preserved, i.e., the edge atoms of hexagon structures in the corner get the relatively major bond contractions with respect to the 2H-$AsTe_2$ QDs. The corner-to-corner lengths of the smallest and the largest size 1T-$AsTe_2$ QDs are, respectively, ~6.3 and 19 Å. In very small size QD flakes of 1T-$AsTe_2$ structure (see $1^{st}$ and $2^{nd}$ QD flakes in Figure 6), the HOMO-LUMO energy gaps are found because of the quantum confinement effect. Although the band gap is tunable by small size, the HOMO-LUMO are degenerate on Fermi level in relatively larger size shape of the 1T-$AsTe_2$ QDs which is smaller than experimentally obtained the smallest QD flakes. Hence, it is found that 1T-$AsTe_2$ QD flakes are quite robust metallic materials as well.

It should be remarked that the most of the QDs of the $AsTe_2$ phases are found to be nonmagnetic. However, the ground state energy differences between nonmagnetic and magnetic states are found quite small in some QD flakes, hence, nonmagnetic ground state structures are used in all calculations. The metallic character of $AsTe_2$ phases depending on their shape, size, and edge reconstruction keeps the promise of the vast variety of applications in nanoelectronic devices.

## 6. Concluding Remarks

The structural, phononic, and electronic properties of 2H-$AsTe_2$ and 1T-$AsTe_2$ monolayer structures were investigated based on first-principles calculations within DFT. It was found that both of 2H-$AsTe_2$ and 1T-$AsTe_2$ compounds are the dynamically stable ultra-thin materials that can be fabricated as a free-standing form. In addition, the both of $AsTe_2$ monolayers were found as electronically metallic materials. Furthermore, the electronic properties of 2H and 1T-$AsTe_2$ were negligible changed by applying biaxial strain, namely, both of them were obtained the ultra-thin robust metallic materials. It was found that small size NR and QD flakes of 2H-$AsTe_2$ and 1T-$AsTe_2$ structures preserve the electronically robust metallic character as well.

Since 2H and 1T phases are common structures in 2D TMDs, the both of structures of $AsTe_2$ monolayer can be used as the non-gold contact for low-cost switching device applications. Owing to their non-magnetic robust metallicity, the investigation electron-phonon coupling and possible evolution of superconducting characteristics[68,69] of $AsTe_2$ monolayers under confinement can be an attractive topic for future studies.

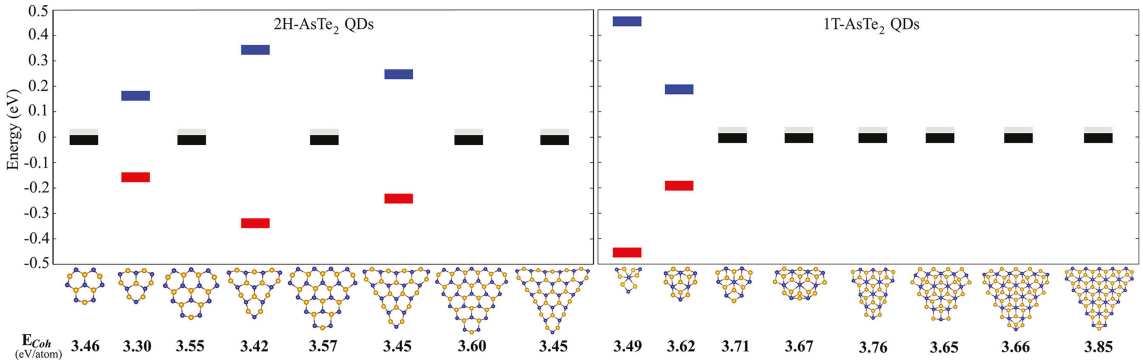


**Figure 6.** (Color online) The energy levels, HOMO - LUMO gaps of QDs of the $AsTe_2$ phases. The insets show the top view representation of the QDs of the $AsTe_2$ phases. The size of QDs increases properly as X axis. The red line and blue lines represent, respectively, HOMO and LUMO states of QDs of the $AsTe_2$ phases. The half grey and half black line represents the vanishing of the HOMO-LUMO gaps of QDs of the $AsTe_2$ phases. The cohesive energy of each QD flake is shown under corresponding top view representation of the QDs of the $AsTe_2$ phases.

## Acknowledgment

*Computer time has been granted by TUBITAK ULAKBIM, High Performance and Grid Computing Center (TR-Grid e-Infrastructure). HS acknowledges financial support from the TUBITAK under the project number 117F095. HS acknowledges support from Türkiye Bilimler Akademisi-Turkish Academy of Sciences under the GEBIP program.*

## Conflict of Interest

The authors declare no conflict of interest.

**Keywords:** Arsenic ditelluride monolayers · 2D materials · metal quantum dots · nanoribbons · ultra-thin metals

[1] K. S. Novoselov, A. K. Geim, S. V. Morozov, D. Jiang, Y. Zhang, S. V. Dubonos, I. V. Grigorieva, A. A. Firsov, *Science* **2004**, *306*, 666–669.
[2] A. K. Geim, K. S. Novoselov, *Nat. Mater.* **2007**, *6*, 83–191.
[3] D. Pacile, J. C. Meyer, Ç. Ö. Girit, A. Zettl, *Appl. Phys. Lett.* **2008**, *92*, 133107.
[4] W. Q. Han, L. Wu, Y. Zhu, K. Watanabe, T. Taniguchi, *Appl. Phys. Lett.* **2008**, *93*, 223103.
[5] K. K. Kim, A. Hsu, X. Jia, S. M. Kim, Y. Shi, M. Hofmann, D. Nezich, F. Rodriguez-Nieva, M. Dresselhaus, T. Palacios, J. Kong, *Nano Lett.* **2012**, *12*, 161–166.
[6] S. Cahangirov, M. Topsakal, E. Aktürk, H. Sahin, S. Ciraci, *Phys. Rev. Lett.* **2009**, *102*, 236804.
[7] P. Vogt, P. Padova, C. Quaresima, J. Avila, E. Frantzeskakis, M. C. Asensio, A. Resta, B. Ealet, G. L. Lay, *Phys. Rev. Lett.* **2012**, *108*, 155501.
[8] S. Manzeli, D. Ovchinnikov, D. Pasquier, O. V. Yazyev, A. Kis, *Nat. Rev. Mater* **2017**, *2*, 17033.
[9] J. N. Coleman, M. Lotya, A. O'Neill, S. D. Bergin, P. J. King, U. Khan, Young, A. Gaucher, S. De, R. J Smith, I. V. Shvets, S. K. Arora, G. Stanton G, H. Y. Kim, K. Lee, G. T. Kim, G. S. Duesberg, T. Hallam, J. J. Boland, J. J. Wang, J. F. Donegan, J. C. Grunlan, G. Moriarty, A. Shmeliov, R. J. Nicholls, J. M. Perkins, E. M. Grieveson, K. Theuwissen, D. W. McComb, P. D. Nellist, V. Nicolosi, *Science* **2011**, *331*, 568–571.
[10] M. Chhowalla, H. S. Shin, G. Eda, L. J. Li, K. P. Loh, H. Zhang, *Nat. Chem* **2013**, *5*, 263–275.
[11] B. Chen, H. Sahin, A. Suslu, L. Ding, M. I. Bertoni, F. M. Peeters, S. Tongay, *ACS Nano* **2015**, *9*, 5326–5332.
[12] X. Huang, S. Tang, X. Mu, Y. Dai, G. Chen, Z. Zhou, F. Ruan, Z. Yang, N. Zheng, *Nat. Nanotechnol* **2011**, *6*, 28–32.
[13] H. Duan, N. Yan, R. Yu, C. -R. Chang, G. Zhou, H.-S. Hu, H. Rong, Z. Niu, J. Mao, H. Asakura, T. Tanaka, P. J. Dyson, J. Li, Y. Li, *Nat. Commun* **2014**, *5*, 3093.
[14] H. Liu, A. T. Neal, Z. Zhu, Z. Luo, X. Xu, D. Tomane, P. D. Ye, *ACS Nano* **2014** *8*, 4033–4041.
[15] A. Carvalho, M. Wang, X. Zhu, A. S. Rodin, H. Su, A. H. C. Neto, *Nat. Rev. Mater.* **2016**, *1*, 16061.
[16] Z. Zhu, D. Tomanek, *Phys. Rev. Lett.* **2014**, *112*, 176802.
[17] S. Zhang, S. Guo, Z. Chen, Y. Wang, H. Gao, J. Gmez-Herrero, P. Ares, F. Zamora, Z. Zhu, H. Zeng, *Chem Soc Rev.* **2018**, *47*, 982–1021.
[18] S. Zhang, M. Xie, F. Li, Z. Yan, Y. Li, E. Kan, W. Liu, Z. Chen, H. Zeng, *Angew Chem Int Ed Engl.* **2016**, *55*, 1666–1669.
[19] J. Ji, X. Song, J. Liu, Z. Yan, C. Huo, S. Zhang, M. Su, L. Liao, W. Wang, Z. Ni, Y. Hao, H. Zeng, *Nat. Commun* **2016**, *7*, 13352.
[20] D. Voiry, H Yamaguchi, J. W. Li, R. Silva, D. C. B. Alves, T. Fujita, M. W. Chen, T. Asefa, V. B. Shenoy, G. Eda, M. Chhowalla, *Nat. Mater.* **2013**, *12*, 850–855.
[21] P. K. Jain, X. Huang, I. H. El-Sayed, M. A. El-Sayed, *Acc. Chem. Res.* **2008**, *41*, 1578–1586.
[22] A. J. Gallanta, M. A. Kaliteevski, D. Wood, M. C. Petty, R. A. Abram, S. Brand, G. P. Swift, D. A. Zeze, J. M. Chamberlain, *Appl. Phys. Lett.* **2007**, *91*, 161115.
[23] A. J. Gallant, M. A. Kaliteevski, S. Brand, D. Wood, M. Petty, R. A. Abram, J. M. Chamberlaina, *J. Appl. Phys.* **2007**, *102*, 023102.
[24] J. H. Sung, H. Heo, S. Si, Y. H. Kim, H. R. Noh, K. Song, J. Kim, C. S. Lee, S. Y. Seo, D. H. Kim, H. K. Kim, H. W. Yeom, T. H. Kim, S. Y. Choi, J. S. Kim, M. H. Jo, *Nat. Nano.* **2017**, *12*, 10641070.
[25] J. Zhao, Q. Deng, A. Bachmatiuk, G. Sandeep, A. Popov, J. Eckert, M. H. Ruemmeli, *Science* **2014**, *343*, 1228–1232.
[26] J. E. Padilha, R. H. Miwa, Antonio J. R. da Silva, A. Fazzio, *Phys. Rev. B* **2017**, *95*, 195143.
[27] Y. He, C. D. Spataru, F. Lonard, R. E. Jones, M. E. Foster, M. D. Allendorfa, A. A. Talin, *Phys. Chem. Chem. Phys.* **2017**, *29*, 19461–19467.
[28] X. Kleber, L. Simonet, F. Fouquet, M. Delnondedieu, *Modelling Simul. Mater. Sci. Eng.* **2006**, *14*, 21–31.
[29] Y. Saito, T. Nojima, Y. Iwasa, *Nat. Rev. Mater.* **2016**, *2*, 16094.
[30] G. S. Nolas, J. Sharp, J. Goldsmid, *Thermoelectrics*, (Eds.; Springer:) Berlin, **2001**.
[31] H. Scherrer, S. Scherrer, *In Thermoelectrics Handbook: Macro to Nano; D. M. Rowe*, (Ed.; CRC Press:) Boca Raton, FL, **2015**
[32] H. Zhang, C. X. Liu, X. L. Qi, X. Dai, Z. Fang, S. C. Zhang, *Nat. Phys.* **2009**, *5*, 438–442.
[33] D. Hsieh, Y. Xia, D. Qian, L. Wray, F. Meier, J. H. Dil, J. Osterwalder, L. Patthey, A. V. Fedorov, H. Lin, A. Bansil, D. Grauer, Y. S. Hor, R. J. Cava, M. Z. Hasan, *Phys. Rev. Lett.* **2009**, *103*, 146401.
[34] V. V. Brazhkin, E. Bychkov, O. B. Tsiok, *Phys. Rev. B* **2017**, *95*, 054205.
[35] N. S. Platakis, H. C. Gatos, *Physica Status Solidi A* **1972**, *13*, K1–K4.
[36] J. Zhao, L. Yang, Z. Yu, Y. Wang, C. Li, K. Yang, Z. Liu, Y. Wang, *Inor. Chem.* **2016**, *55*, 3907–3914.
[37] C. Morin, S. Corallini, J. Carreaud, J. B Vaney, G. Delaizir, J. C Crivello, E. B. Lopes, A. Piarristeguy, J. Monnier, C. Candolfi, V. Nassif, G. J. Cuello, A. Pradel, A. P. Goncalves, B. Lenoir, E. Alleno, *Inor. Chem.* **2015**, *54*, 9936–9947.
[38] J. B. Vaney, J. Carreaud, G. Delaizir, C. Morin, J. Monnier, E. Alleno, A. Piarristeguy, A. Pradel, A. P. Gonalves, E. B. Lopes, *J. Electron. Mater.* **2016**, *45*, 1447–1452.
[39] T. J. Scheidemantel, J. F. Meng, J. V. Badding, *J. Phys. Chem. Solids.* **2005**, *66*, 1744–1747.
[40] J. B. Vaney, J. Carreaud, G. Delaizir, A. Pradel, A. Piarristeguy, C. Morin, E. Alleno, J. Monnier, A. P. Goncalves, C. Candolfi, A. Dauscher, B. Lenoir, *Adv. Electron. Mater.* **2015**, *1*, 1400008.
[41] M. Burzo, P. Komarov, P. Raad, *IEEE CPMT* **2003**, *26*, 80–88.
[42] A. Delan, M. Rennau, S. E. Schulz, T. Gessner, *Microelectronics Engineering* **2003**, *70*, 280–284.
[43] L. Mochalov, A. Nezhdanov, D. Usanov, A. Markelov, V. Trushin, G. Chidichimo, G. De Filpo, D. Gogova, A. Mashin, *Superlattice. Microst.* **2017**, *111*, 173–180.
[44] L. Mochalov, A. Nezhdanov, A. Strikovskiy, M. Gushin, G. Chidichimo, G. Filpo, A. Mashin, *Opt. Quant. Electron.* **2017**, *8*, 274.
[45] L. Mochalov, A. Nezhdanov, M. Kudryashov, A. Logunov, A. Strikovskiy, M. Gushchin, G. Chidichimo, G. Filpo, A. Mashin, *Plasma Chem. Plasma Process.* **2017**, *7*, 1417–1429.
[46] L. Mochalov, D. Dorosz, A. Nezhdanov, M. Kudryashov, S. Zelentsov, D. Usanov, A. Logunov, A. Mashina, D. Gogova, *Spectrochim. Acta A* **2018**, *191*, 211–216.
[47] V. P. Cuenca-Gotor, J. A. S. Tresserras, J. Ibaez, C. Popescu, O. Gomis, R. Vilaplana, F. J. Manjn, A. L. Liceranzu, E. Sagasta, A. S. Alcubilla, I. G. Gurtubay, M. Mollar, A. Bergara, *J. Phys. Chem. C* **2016**, *120*, 19340–19352.
[48] M. A. Lukowski, A. S. Daniel, F. Meng, A. Forticaux, L. S. Li, S. Jin, *J. Am. Chem. Soc.* **2013**, *135*, 10274–10277.
[49] G. Kresse, J. Hafner, *Phys. Rev. B* **1993**, *47*, 558–561.
[50] G. Kresse, J. Furthmüller, *Phys. Rev. B* **1996**, *54*, 11169–11186.
[51] J. P. Perdew, A. Zunger, *Phys. Rev. B* **1981**, *23*, 5048–5079.
[52] D. M. Ceperley, B. J. Alder, *Phys. Rev. Lett.* **1980**, *45*, 566–569.
[53] G. Henkelman, A. Arnaldsson, H. Jonsson, *Comput. Mater. Sci.* **2016**, *36*, 354–360.
[54] D. Alfe, *Comp. Phys. Commun.* **2009**, *180*, 2622–2633.
[55] Y. J. Yu, Y. Zhao, S. Ryu, L. E. Brus, K. S. Kim, P. Kim, *Nano Lett.* **2009**, *9*, 3430–3434.
[56] A. M. Snchez, L. Wirtz, *Phys. Rev. B* **2011**, *84*, 155413.
[57] F. Liu, P. Ming, J. Li, *Phys. Rev. B* **2007**, *76*, 064120.
[58] G. Cassabois, P. Valvin, B. Gil, *Nat. Photonics.* **2016**, *10*, 262266.
[59] M. D. Bartlett, N. Kazem, M. J. Powell-Palm, X. Huang, W. Sun, J. A. Malen, C. Majidi, *Proc Natl Acad Sci U S A.* **2017**, *114*, 2143–2148.
[60] Y. Li, Z. Zhou, S. Zhang, Z. Chen, *J. Am. Chem. Soc.* **2008**, *130*, 16739.
[61] D. A. Abanin, P. A. Lee, L. S. Levitov, *Phys. Rev. Lett.* **2006**, *96*, 176803.

[62] V. Barone, O. Hod, G. E. Scuseria, *Nano Lett.* **2006**, *6*, 2748–2754.
[63] L. L. Song, X. H. Zheng, R. L. Wang, Z. Zeng, *J. Phys. Chem. C* **2010**, *114*, 12145–12150.
[64] D. Q. Fang, Y. Zhang, S. L. Zhang, *New J. Phys.* **2014**, *16*, 115006.
[65] E. Janssens, H. Tanaka, S. Neukermans, R. E. Silverans, P. Lievens, *New. J. Phys.* **2003**, *5*, 46.
[66] S. M. Reimann, M. Koskinen, H. Hakkinen, P. E. Lindelof, M. Manninen, *Phys. Rev. B* **1997**, *56*, 12147–12150.
[67] M. Brack, J. Blaschke, S. C. Greagh, A. G. Magner, P. Meier, S. M. Reimann *Z. Phys. D* **1997**, *40*, 276–281.
[68] Q. H. Chen, J. M. Lu, L. Liang, O. Zheliuk, A. Ali, P. Sheng, J. T. Ye, *Phys. Rev. Lett.* **2017**, *119*, 147002.
[69] J. Bekaert, A. Aperis, B. Partoens, P. M. Oppeneer, M. V. Milosevic, *Phys. Rev. B* **2017**, *96*, 094510.

Manuscript received: May 17, 2018
Accepted Article published: June 26, 2018
Version of record online: August 1, 2018